Near-infrared optical properties and proposed phase-change usefulness of transition metal disulfides

View Online   Export Citation   CrossMark

Akshay Singh,[1] (iD) Yifei Li,[1] Balint Fodor,[2] Laszlo Makai,[2] Jian Zhou,[3] Haowei Xu,[4] Austin Akey,[5] Ju Li,[1,4]
and R. Jaramillo[1,a] (iD)

AFFILIATIONS

[1]Department of Materials Science and Engineering, Massachusetts Institute of Technology, Cambridge, Massachusetts 02139, USA
[2]Semilab Semiconductor Physics Laboratory Co. Ltd., Budapest 1117, Hungary
[3]Center for Advancing Materials Performance from the Nanoscale, State Key Laboratory for Mechanical Behavior of Materials,
 Xi'an Jiaotong University, Xi'an 710049, China
[4]Department of Nuclear Science and Engineering, Massachusetts Institute of Technology, Cambridge, Massachusetts 02139, USA
[5]Center for Nanoscale Systems, Harvard University, Cambridge, Massachusetts 02138, USA

[a]rjaramil@mit.edu

ABSTRACT

The development of photonic integrated circuits would benefit from a wider selection of materials that can strongly control near-infrared (NIR) light. Transition metal dichalcogenides (TMDs) have been explored extensively for visible spectrum optoelectronics; the NIR properties of these layered materials have been less-studied. The measurement of optical constants is the foremost step to qualify TMDs for use in NIR photonics. Here, we measure the complex optical constants for select sulfide TMDs (bulk crystals of MoS_2, TiS_2, and ZrS_2) via spectroscopic ellipsometry in the visible-to-NIR range. We find that the presence of native oxide layers (measured by transmission electron microscopy) significantly modifies the observed optical constants and need to be modeled to extract actual optical constants. We support our measurements with density functional theory calculations and further predict large refractive index contrast between different phases. We further propose that TMDs could find use as photonic phase-change materials, by designing alloys that are thermodynamically adjacent to phase boundaries between competing crystal structures, to realize martensitic (i.e., displacive, order–order) switching.

Integrated photonics offers a way to create all-optical circuits to reduce the power needed to move and process massive data flows and to move beyond-von Neumann computing.[1,2] Essential for photonic circuits are active materials that can modulate the phase and amplitude of light to perform switching, logic, and signal processing; if these changes are nonvolatile, then they can also be used for memory. The interaction length required to produce a substantial modulation of the optical phase is $L \sim \lambda_0/\Delta n$, where λ_0 is the free-space wavelength and Δn is the refractive index change. For instance, well established photonic material $LiNbO_3$ produces Δn of order 0.001 at typical supply voltages for electro-optic modulation and therefore requires a large interaction length $L > 1$ mm. A leading class of active materials that can strongly modulate near-infrared (NIR) light on a sub-micrometer length scale are the so-called phase-change chalcogenides, such as

those found in the Ge-Sb-Te (GST) system.[3] These materials operate by switching between crystalline and amorphous phases, which produce refractive index changes $\Delta n > 1$, but suffer from high optical losses in the NIR and sub-gigahertz phase-change operation.[4–6] There is a need to expand the selection of materials available for phase-change functionality in the NIR for integrated photonics.

Transition metal dichalcogenides (TMDs) are layered materials (van der Waals-bonded solids) with intriguing physical properties that include layer-number-dependent bandgap, electron pseudospin, exciton and trion excitations, chemical tunability, catalytic action, polymorphism and phase-change behavior, and strong above-bandgap light absorption.[7–15] The NIR and below-bandgap optical properties of TMDs have been little-studied.[16–19] TMDs interact strongly with light and are expected to feature low-loss for below-bandgap wavelengths.

Polymorphism suggests that transitions between structural phases, such as the trigonal prismatic 2H and octahedral 1T (or distorted 1T' and $1T_d$) may be useful for optical switching.[20,21] Transitions between 2H and 1T can be described by a simple translation of a plane of chalcogen atoms (a martensitic transformation).[22] The layered, van der Waals crystal structure suggests that martensitic transformation strain may be low, which is beneficial for switching energy and fatigue. Phase-change functionality (i.e., transformation between layered polymorphs) at room-temperature has been demonstrated for tellurides including $MoTe_2$ and (Mo, W)Te_2.[21,23–25]

In this manuscript, we focus on sulfide TMDs, because they have the largest bandgap (relative to selenides and tellurides) and therefore offer the largest spectral range for low-loss, below-bandgap operation. Unfortunately, the energetic cost of switching between phases is also highest for pure sulfides (relative to selenides and tellurides).[23,26] We propose that alloying sulfide TMDs with different equilibrium structural phases, such as 2H MoS_2 and 1T TiS_2, could enable low-power switching. Specifically, these alloyed materials can be designed to be adjacent to a thermodynamic phase boundary.

Here, we measure the complex relative permittivity ($\epsilon = \epsilon_1 - i\epsilon_2$) of 2H-$MoS_2$, 1T-$ZrS_2$, and 1T-$TiS_2$ bulk crystals in the visible-to-NIR region (300–2100 nm), using spectroscopic ellipsometry (SE). We find that ϵ in the NIR cannot be simply extracted by extrapolating from visible-light measurements and requires explicit measurements. We find that spectroscopic measurements must account for the presence of native oxide to avoid overestimating NIR loss. We support our measurements with density functional theory (DFT) calculations, which further predict a large refractive index contrast between 2H and 1T phases. We then suggest a paradigm to use TMD alloys as active phase-change materials for integrated photonics and use DFT to calculate alloy phase stability.

Ellipsometry is a nondestructive optical technique that is widely used to measure the optical constants of thin films and bulk crystals.[27,28] The technique involves measuring the ellipsometric ratio (ρ) of the amplitude reflection Fresnel coefficients for P- and S-polarized light (r_P and r_S, respectively) incident on a smooth surface. ρ is written as

$$\rho = \frac{r_P}{r_S} = \tan(\psi) \exp(i\Delta), \quad (1)$$

where ψ and Δ are the ellipsometric angles. ρ is a complex number and can be used to directly calculate real and imaginary optical constants, without relying on Kramers–Kronig (KK) relations. Relying on KK-constrained data can result in erroneous results, due to the extension of KK integral into spectral regions where measurements were not performed. Previous measurements have partially-characterized 2H-MoS_2 bulk crystals and thin films, with limited information in the NIR.[29–33] Much less information is available for 1T-ZrS_2 and 1T-TiS_2.[34]

We use thick TMD crystals to directly measure the dielectric properties in the NIR, without relying on models or extrapolation from visible-light measurements. For sufficiently-thick crystals, the light is absorbed completely, and there are no reflections from the back surface that can mix polarizations and cause measurement errors. We perform measurements on the mirrorlike faces of the as-received crystals, without any surface processing steps; below, we discuss how we account for the inevitable native oxide layer. We use two different

ellipsometry instruments (Semilab SE-2000, and J. A. Woollam UV-NIR Vase) to ensure repeatability (see the supplementary material for details).

The procedure for extracting ϵ from measurements of ρ is greatly simplified by using bulk crystal, as opposed to thin films. For a bulk, isotropic material, ϵ can be directly calculated as

$$\epsilon = \sin^2(\Phi) * \left(1 + \tan^2(\Phi) * \left(\frac{1 - \rho}{1 + \rho} \right)^2 \right), \quad (2)$$

where $\epsilon = \epsilon_1 - i\epsilon_2$, and Φ is the angle of incidence (AOI) relative to the surface normal direction.[27] ϵ calculated using Eq. (2) is called the "effective" permittivity and corresponds to a model of a pristine material interface with air, without a native oxide or any other overlayer. The presence of a native oxide can produce substantial errors including an overestimation of optical loss, as discussed below and in the supplementary material.

We use the results of DFT electronic structure calculations to predict dielectric functions using the random phase approximation, as described in the previous work and in the supplementary material.[35,36] Briefly, we use Vienna ab initio simulation package (VASP), version 5.4.[37–40] We treat the core and valence electrons by the projector-augmented plane wave method and approximate the exchange-correlation interaction by the generalized gradient approximation functional, implemented in the Perdew-Burke-Ernzerhof form.[41,42] The energy minimization and force convergence criteria are 10^{-7} eV and 10^{-3} eV/Å, respectively.

The presence of a native oxide layer affects the experimental results in the entire spectral range and particularly for regions where the optical loss of the TMD is expected to be small, such as below the bandgap of MoS_2 and ZrS_2. We directly measured the thickness and composition of the native oxide using cross-sectional transmission electron microscopy (TEM) (see the supplementary material). On MoS_2, we find a rough surface, possibly including a native oxide, approximately 2 nm thick. On ZrS_2, we find a native oxide layer nearly 20 nm thick; similarly thick native oxide layers have been observed on $ZrSe_2$.[43] On TiS_2, we saw no native oxide, within the imaging resolution of our experiment (∼1 nm). Adding these overlayers to the optical model used to analyze the ellipsometry data significantly affects the extracted permittivity of MoS_2 and ZrS_2 (see the supplementary material for modeling details).

In Fig. 1, we present the experimentally-measured and theoretically-calculated in-plane complex permittivities for MoS_2, TiS_2, and ZrS_2. The experimental data in Fig. 1 indicate the actual permittivity, determined by analyzing the ellipsometry data taking into account the native oxide layers. Of particular relevance for NIR photonics, ϵ_1 is large below the bandgap of MoS_2 and ZrS_2 (indirect E_g = 1.1 and 1.6 eV, respectively, indicated by solid gray lines); TiS_2 is a semimetal, (bandgap < 0.5 eV).[18,34,44] The DFT calculations match fairly well the experimental data, both in magnitude and in spectral position of individual features. The A, B, and C excitons of MoS_2 are well-resolved.[45] For TiS_2, the experimentally-observed peaks match in energy but are substantially broader than those calculated by DFT and are qualitatively similar to previously-reported measurements of $TiSe_2$, indicating similar physical origins of the optical transitions.[17] In ZrS_2, the strongest direct gap excitonic oscillators (2.5 and 2.9 eV) are observed in both experiment and theory, although the experimental
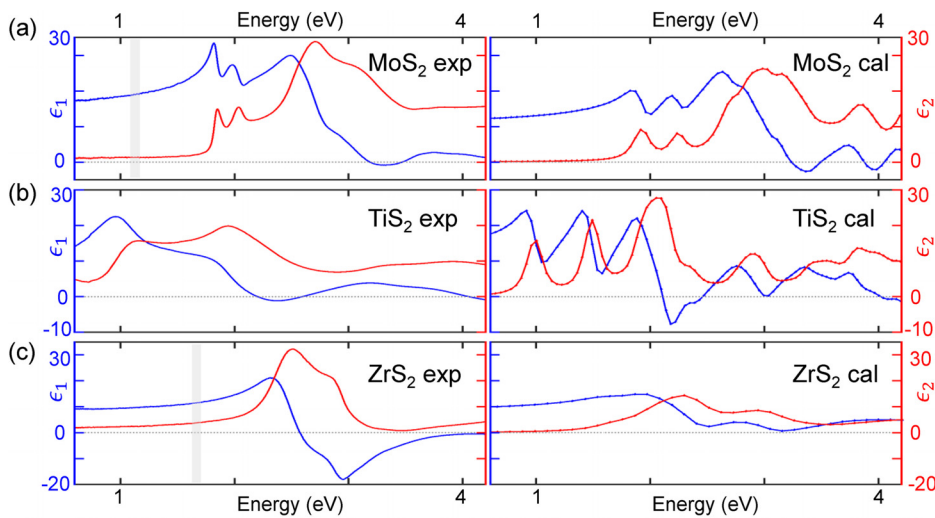
FIG. 1. NIR-VIS complex relative permittivity (ϵ) of sulfide TMDs. (Left column) Experimentally-measured permittivity at room-temperature and AOI = 70° by spectroscopic ellipsometry. (Right column) Calculated by DFT. Results shown for (a) 2H-MoS$_2$, (b) 1T-TiS$_2$, and (c) 1T-ZrS$_2$. The indirect bandgap of MoS$_2$ and ZrS$_2$ is indicated by light-gray lines.

data do not show the lowest-lying indirect gap transition near E_g. The 2.5 and 2.9 eV transitions are sufficiently close in energy to create zero-crossing of ϵ_1 near 3.2 eV, which is not seen in the DFT calculations. Further discussion of the various optical transitions can be found in the supplementary material. Cross-polarization components are explicitly measured through generalized ellipsometry and are found to be ~0 for TiS$_2$ and MoS$_2$ (see the supplementary material).

The complex refractive index ($n - ik$) is related to ϵ by

$$n = real\left(\sqrt{\epsilon}\right), \quad k = -imaginary\left(\sqrt{\epsilon}\right). \quad (3)$$

k is related to the absorption coefficient ($\alpha = 4\pi k/\lambda$). In Fig. 2, we plot experimentally-measured n and k in the NIR spectral region 0.6–1.5 eV (827–2067 nm). All three materials have large n, comparable to or larger than that of silicon ($n_{NIR} \approx 3.4$), which is appealing for guiding NIR light. MoS$_2$ and ZrS$_2$ are indirect-bandgap semiconductors and have low-loss in the NIR. TiS$_2$ is semimetallic and has higher loss.

The loss coefficients (k) determined by experiment and reported in Fig. 2 are conditional on the particular samples measured and on our optical modeling and should be considered upper-bounds for these materials. In Fig. 2, we indicate k determined from the effective permittivity [Eq. (3)], assuming no native oxide (dashed lines) and the value determined by optical modeling including native oxide thickness determined by TEM (solid lines). Taking the native oxide into account results in a lower value of the determined loss. Another important variable is the presence of defects, which contribute to below-bandgap absorption and optical loss. Our samples are bulk crystals (including a naturally-occurring specimen of MoS$_2$) and definitely contain defects, including sulfur vacancies that contribute to NIR absorption.[46] Measurements on synthetic MoS$_2$ monolayers have shown lower loss in the NIR.[32,33] Our theoretical calculations are performed using models of perfect, defect-free crystals and predict substantially lower loss than the experiments (see Fig. 1). As the science of processing TMD materials improves, we will gain greater control over defects and can expect to have very low-loss TMDs for NIR applications.

We now address the question of the usefulness of phase change in sulfide TMDs as functionality for active materials. In Fig. 3, we

show the calculated refractive index difference (Δn) between the 2H and 1T' phases of bulk MoS$_2$. We here show results for the 1T' phase instead of 1T because, according to our DFT calculations, 1T' has lower energy than 1T for monolayer MoS$_2$ and therefore 1T may spontaneously relax to 1T' in the zero-temperature limit. Compared to the 1T phase, the 1T' phase has lower in-plane symmetry due to Mo–Mo dimerization, leading to optical trirefringence. In Fig. 3, we have averaged the results for the principal in-plane axes for consistency with the experimental literature, in which there is little evidence for strong in-plane anisotropy at room-temperature (this could be due to ferroelastic domain microstructure, or a reduced order parameter at relatively high temperature). We find that Δn is large, comparable to or larger than that realized by phase-change materials in the GST system. The theoretically-predicted spectral features suggest photonics-relevant $\Delta n \sim 1$ throughout the NIR.
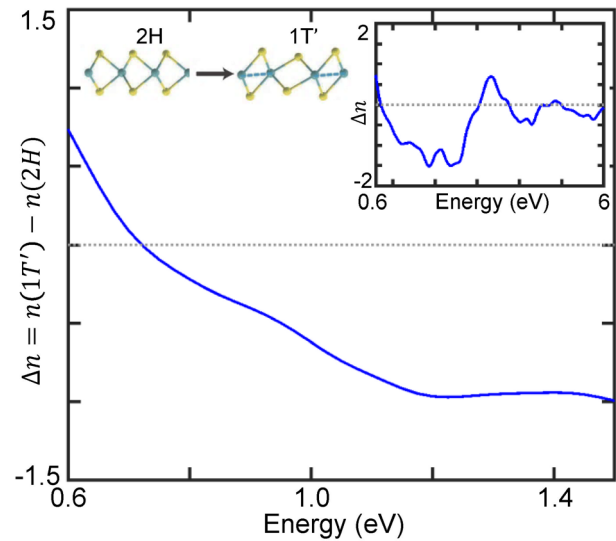
We focus on the NIR optical properties of sulfide TMDs because they offer lower optical loss (in NIR) than their selenide and telluride cousins, which have smaller bandgap. Unfortunately, the energetic cost of switching between phases is also highest for pure sulfides.[23,25] Alloying sulfide TMDs with different reference states could enable low-power switching. The thermodynamics of TMD alloys are not well-established, and no phase diagrams have been published for the MoS$_2$-TiS$_2$-ZrS$_2$ ternary system, or the subsidiary binary systems. Here, we use DFT calculations to evaluate the likelihood of making binary alloys near the 2H-1T phase boundary (see the supplementary material for calculation details).

In Fig. 4, we show the calculated Gibbs free energy-composition curves for the MoS$_2$-TiS$_2$ and MoS$_2$-ZrS$_2$ systems at 300 K. The results are very similar at 1000 K (not shown here), although with an overall downward shift of ~1 eV/f.u (formula unit) relative to the data at 300 K. For both systems, the free energy curves for the 2H and 1T phases cross at an intermediate composition, which is suggestive of a phase boundary. For the MoS$_2$-TiS$_2$ system, the curves are concave-downward and lie above the convex hull, which for this system is a straight line connecting the pure phases. Therefore, MoS$_2$-TiS$_2$ alloys will have a tendency to phase-separate at equilibrium. For the MoS$_2$-ZrS$_2$, we predict a solid solution in the 2H structure for Mo$_x$Zr$_{1-x}$S$_2$, $x > 0.75$, and phase
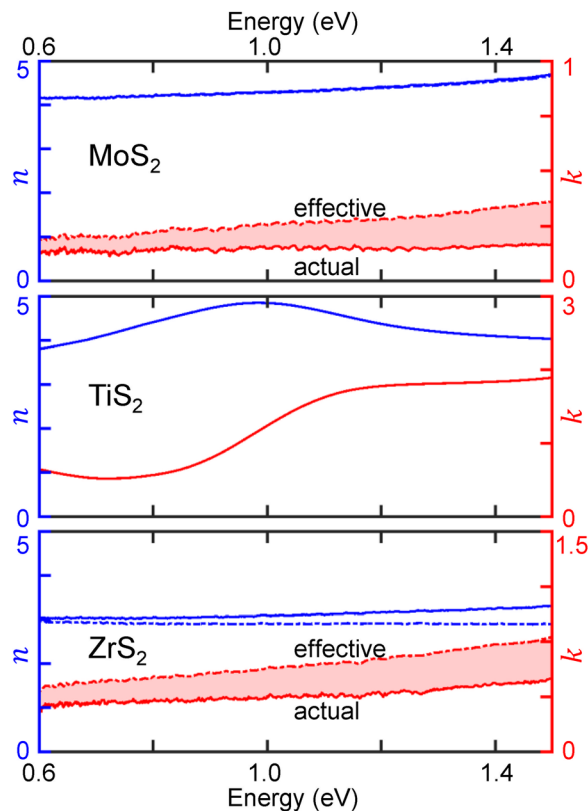
FIG. 2. Experimentally-measured real (n) and imaginary (k) refractive indexes of MoS_2, TiS_2, and ZrS_2 in the NIR spectral region. The solid lines (labeled "actual") for MoS_2 and ZrS_2 are determined by modeling the ellipsometry data including native oxide layers. The dashed lines (labeled "effective") represent the effective permittivity, which ignores the native oxide. The red shaded area represents experimental uncertainty (in k) due to potential misestimation of the native oxide thickness.

FIG. 3. Theoretically-predicted refractive index difference (Δn) between the 1T' and 2H phases of bulk MoS_2 in the NIR. (Inset, right) Δn over a wider energy range. (Inset, left) Illustrated change of atomic structure for 2H-1T' phase transition.

separation for more Zr-rich compositions. For both of these systems, the relatively small energy difference between the alloy curves and the convex hull (<1 eV/f.u.) suggests that alloys may be kinetically-stabilized near the 2H-1T phase boundary. The ZrS_2-TiS_2 system is likely to be stable as a solid solution in the 1T phase, for which we do not calculate a

significant positive enthalpy of mixing and therefore do not expect to observe spinodal decomposition. Future work should consider metastability and the kinetics of phase separation in TMD alloy systems, and a particular focus on low-temperature processing of TMD alloy thin films.

We measure the complex optical constants of select sulfide TMDs in a spectral range from the visible to the NIR. The samples are single-crystals of 2H-MoS_2, 1T-ZrS_2, and 1T-TiS_2 and are chosen to represent prototypes of the 2H and 1T structure types. All materials have high index of refraction ($n \sim$ 3–4), and MoS_2 and ZrS_2 feature low-loss in the NIR. We find that the presence of native oxides significantly changes the observed optical constants, and these oxide layers need to be characterized and modeled. Further, our DFT calculations predict a large refractive index and strong contrast in optical properties ($\Delta n \sim 1$) between the different structure (phase) types, suggesting a role for TMDs as phase-change materials for integrated photonics. Achieving this goal will require making materials that are thermodynamically-adjacent to a phase boundary. For sulfides, this will likely require
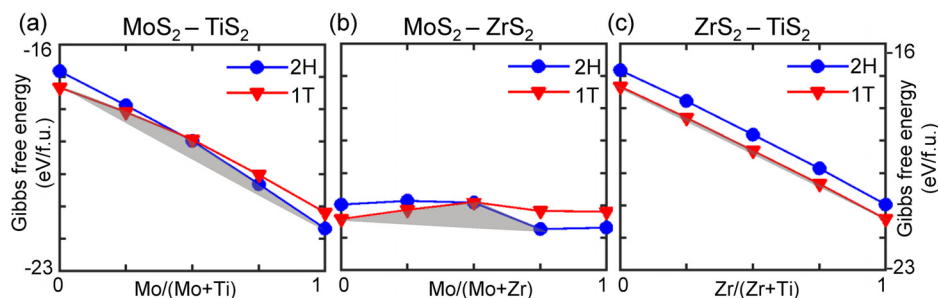
FIG. 4. Theoretically-predicted Gibbs free energy-composition plots for the (a) MoS_2-TiS_2, (b) MoS_2-ZrS_2, and (c) ZrS_2-TiS_2 systems at 300 K. In the first two cases, the alloys are thermodynamically unstable relative to decomposition into pure phases. However, the free energy above the convex hull (gray zone) is small, which suggests that kinetic stabilization will be possible, e.g., through low-temperature processing. ZrS_2-TiS_2 system is expected to form stable alloy solutions. We performed calculations for fully-relaxed structures. Therefore, the phase labeled "1T" in some cases has distortions akin to the 1T' phase.

alloying. We use DFT to calculate free energy-composition curves for alloys of MoS_2, ZrS_2, and TiS_2. The alloy structural phases become energetically degenerate at intermediate compositions, at which martensitic switching may be possible, if the alloys are found to be metastable or kinetically-stable.

See the supplementary material for information on: Experimental setup; attributing peaks to different transitions; transmission electron microscopy (TEM) characterization of surface; energy dispersive X-ray spectroscopy (EDS) of MoS_2 and ZrS_2 top surfaces; oxide and roughness modeling; TiS_2 with and without focusing optics; Mueller matrix (MM) measurements; theoretical calculations (DFT) for out-of-plane relative permittivity; multiple angle of incidence (MAI) measurements; effective ϵ for a range of $\epsilon_\perp$ and $\epsilon_\parallel$, and for different angle of incidence (AOI); density function theory (DFT) calculations; phase diagram calculation; and comparison with previously published data for MoS_2.

REFERENCES

[1] M. Asghari and A. V. Krishnamoorthy, Nat. Photonics **5**, 268 (2011).

[2] Y. Shen, N. C. Harris, S. Skirlo, M. Prabhu, T. Baehr-Jones, M. Hochberg, X. Sun, S. Zhao, H. Larochelle, D. Englund, and M. Soljačić, Nat. Photonics **11**, 441 (2017).

[3] M. Wuttig and N. Yamada, Nat. Mater. **6**, 824 (2007).

[4] N. Yamada, E. Ohno, K. Nishiuchi, N. Akahira, and M. Takao, J. Appl. Phys. **69**, 2849 (1991).

[5] H. S. P. Wong, S. Raoux, S. Kim, J. Liang, J. P. Reifenberg, B. Rajendran, M. Asheghi, and K. E. Goodson, Proc. IEEE **98**, 2201 (2010).

[6] B.-S. Lee, J. R. Abelson, S. G. Bishop, D.-H. Kang, B. Cheong, and K.-B. Kim, J. Appl. Phys. **97**, 093509 (2005).

[7] K. F. Mak, C. Lee, J. Hone, J. Shan, and T. F. Heinz, Phys. Rev. Lett. **105**, 136805 (2010).

[8] A. Splendiani, L. Sun, Y. Zhang, T. Li, J. Kim, C. Y. Chim, G. Galli, and F. Wang, Nano Lett. **10**, 1271 (2010).

[9] Y. Chen, J. Xi, D. O. Dumcenco, Z. Liu, K. Suenaga, D. Wang, Z. Shuai, Y.-S. Huang, and L. Xie, ACS Nano **7**, 4610 (2013).

[10] J. R. Schaibley, H. Yu, G. Clark, P. Rivera, J. S. Ross, K. L. Seyler, W. Yao, and X. Xu, Nat. Rev. Mater. **1**, 16055 (2016).

[11] A. Singh, K. Tran, M. Kolarczik, J. Seifert, Y. Wang, K. Hao, D. Pleskot, N. M. Gabor, S. Helmrich, N. Owschimikow, U. Woggon, and X. Li, Phys. Rev. Lett. **117**, 257402 (2016).

[12] A. Singh, G. Moody, S. Wu, Y. Wu, N. J. Ghimire, J. Yan, D. G. Mandrus, X. Xu, and X. Li, Phys. Rev. Lett. **112**, 216804 (2014).

[13] R. Lv, H. Terrones, A. L. Elías, N. Perea-López, H. R. Gutiérrez, E. Cruz-Silva, L. P. Rajukumar, M. S. Dresselhaus, and M. Terrones, Nano Today **10**, 559 (2015).

[14] K. F. Mak and J. Shan, Nat. Photonics **10**, 216 (2016).

[15] G. Fiori, F. Bonaccorso, G. Iannaccone, T. Palacios, D. Neumaier, A. Seabaugh, S. K. Banerjee, and L. Colombo, Nat. Nanotechnol. **9**, 768 (2014).

[16] N. Syrbu, V. Z. Cebotari, and N. P. Moldoveanu, Jpn. J. Appl. Phys., Part 1 **35**, 6126 (1996).

[17] T. Buslaps, R. L. Johnson, and G. Jungk, Thin Solid Films **234**, 549 (1993).

[18] A. M. Goldberg, A. R. Beal, F. A. Lévy, and E. A. Davis, Philos. Mag. **32**, 367 (1975).

[19] G. Lucovsky, R. M. White, J. A. Benda, and J. F. Revelli, Phys. Rev. B **7**, 3859 (1973).

[20] L. Liu, J. Wu, L. Wu, M. Ye, X. Liu, Q. Wang, S. Hou, P. Lu, L. Sun, J. Zheng, L. Xing, L. Gu, X. Jiang, L. Xie, and L. Jiao, Nat. Mater. **17**, 1108 (2018).

[21] Y. Wang, J. Xiao, H. Zhu, Y. Li, Y. Alsaid, K. Y. Fong, Y. Zhou, S. Wang, W. Shi, Y. Wang, A. Zettl, E. J. Reed, and X. Zhang, Nature **550**, 487 (2017).

[22] Y.-C. Lin, D. O. Dumcenco, Y.-S. Huang, and K. Suenaga, Nat. Nanotechnol. **9**, 391 (2014).

[23] K.-A. N. Duerloo, Y. Li, and E. J. Reed, Nat. Commun. **5**, 4214 (2014).

[24] W. Jin, T. Schiros, Y. Lin, J. Ma, R. Lou, Z. Dai, J.-X. Yu, D. Rhodes, J. T. Sadowski, X. Tong, T. Qian, M. Hashimoto, D. Lu, J. I. Dadap, S. Wang, E. J. G. Santos, J. Zang, K. Pohl, H. Ding, J. Hone, L. Balicas, A. N. Pasupathy, and R. M. Osgood, Phys. Rev. B **98**, 144114 (2018).

[25] F. Zhang, H. Zhang, S. Krylyuk, C. A. Milligan, Y. Zhu, D. Y. Zemlyanov, L. A. Bendersky, B. P. Burton, A. V. Davydov, and J. Appenzeller, Nat. Mater. **18**, 55 (2019).

[26] Y. Xiao, M. Zhou, J. Liu, J. Xu, and L. Fu, Sci. China Mater. **6**, 759 (2019).

[27] H. Fujiwara, *Spectroscopic Ellipsometry: Principles and Applications* (Wiley, 2007).

[28] D. den Engelsen, J. Opt. Soc. Am. **61**, 1460 (1971).

[29] A. R. Beal and H. P. Hughes, J. Phys. C: Solid State Phys. **12**, 881 (1979).

[30] J. W. Park, H. S. So, S. Kim, S.-H. Choi, H. Lee, J. Lee, C. Lee, and Y. Kim, J. Appl. Phys. **116**, 183509 (2014).

[31] D. Li, X. Song, J. Xu, Z. Wang, R. Zhang, P. Zhou, H. Zhang, R. Huang, S. Wang, Y. Zheng, D. W. Zhang, and L. Chen, Appl. Surf. Sci. **421**, 884 (2017).

[32] W. Li, A. G. Birdwell, M. Amani, R. A. Burke, X. Ling, Y.-H. Lee, X. Liang, L. Peng, C. A. Richter, J. Kong, D. J. Gundlach, and N. V. Nguyen, Phys. Rev. B **90**, 195434 (2014).

[33] H.-L. Liu, C.-C. Shen, S.-H. Su, C.-L. Hsu, M.-Y. Li, and L.-J. Li, Appl. Phys. Lett. **105**, 201905 (2014).

[34] S. C. Bayliss and W. Y. Liang, J. Phys. C: Solid State Phys. **15**, 1283 (1982).

[35] J. Zhou, H. Xu, Y. Li, R. Jaramillo, and J. Li, Nano Lett. **18**, 7794 (2018).

[36] M. Gajdoš, K. Hummer, G. Kresse, J. Furthmüller, and F. Bechstedt, Phys. Rev. B **73**, 045112 (2006).

[37] P. Hohenberg and W. Kohn, Phys. Rev. **136**, B864 (1964).

[38] W. Kohn and L. J. Sham, Phys. Rev. **140**, A1133 (1965).

[39] G. Kresse and J. Furthmüller, Phys. Rev. B **54**, 11169 (1996).

[40] G. Kresse and J. Furthmüller, Comput. Mater. Sci. **6**, 15 (1996).

[41] P. E. Blöchl, Phys. Rev. B **50**, 17953 (1994).

[42] J. P. Perdew, K. Burke, and M. Ernzerhof, Phys. Rev. Lett. **77**, 3865 (1996).

[43] M. J. Mleczko, C. Zhang, H. R. Lee, H.-H. Kuo, B. Magyari-Köpe, R. G. Moore, Z.-X. Shen, I. R. Fisher, Y. Nishi, and E. Pop, Sci. Adv. **3**, e1700481 (2017).

[44] D. L. Greenaway and R. Nitsche, J. Phys. Chem. Solids **26**, 1445 (1965).

[45] J. A. Wilson and A. D. Yoffe, Adv. Phys. **18**, 193 (1969).

[46] F. Fabbri, E. Rotunno, E. Cinquanta, D. Campi, E. Bonnini, D. Kaplan, L. Lazzarini, M. Bernasconi, C. Ferrari, M. Longo, G. Nicotra, A. Molle, V. Swaminathan, and G. Salviati, Nat. Commun. **7**, 13044 (2016).

Supplementary Information for "*Near-infrared optical properties and proposed phase-change usefulness of transition metal disulfides*"

Akshay Singh,[1] Yifei Li,[1] Balint Fodor,[2] Laszlo Makai,[2] Jian Zhou,[3] Haowei Xu,[4] Austin Akey,[5] Ju Li,[4] R. Jaramillo[1*]

1. Department of Materials Science and Engineering, Massachusetts Institute of Technology, Cambridge, MA, 02139, USA.

2. Semilab Semiconductor Physics Laboratory Co. Ltd., Budapest, Hungary

3. Center for Advancing Materials Performance from the Nanoscale, State Key Laboratory for Mechanical Behavior of Materials, Xi'an Jiaotong University, Xi'an 710049, China

4. Department of Nuclear Science and Engineering, Massachusetts Institute of Technology, Cambridge, MA, 02139, USA.

5. Center for Nanoscale Systems, Harvard University, Cambridge, Massachusetts 02138, USA

* rjaramil@mit.edu

S1. Experimental setup

Ellipsometry measurements were performed with two instruments, a SE-2000 from Semilab and a UV-NIR Vase from J. A. Woolam. The Semilab SE-2000 uses a rotating compensator configuration as shown in **Figure S1(a)** and consists of the following elements in consecutive order: broadband white light source, polarizer, rotating compensator, micro-spot objective projecting the light onto the sample, analyzer, and detector (CCD-based multi-channel for visible light; InGaAs photodiode array for NIR light). The Woollam Vase uses a rotating analyzer geometry, and an auto-retarder which functions analogous to a compensator. The focusing optics have a spot size of $\sim 300~\mu$m at 70° angle of incidence (*AOI*).
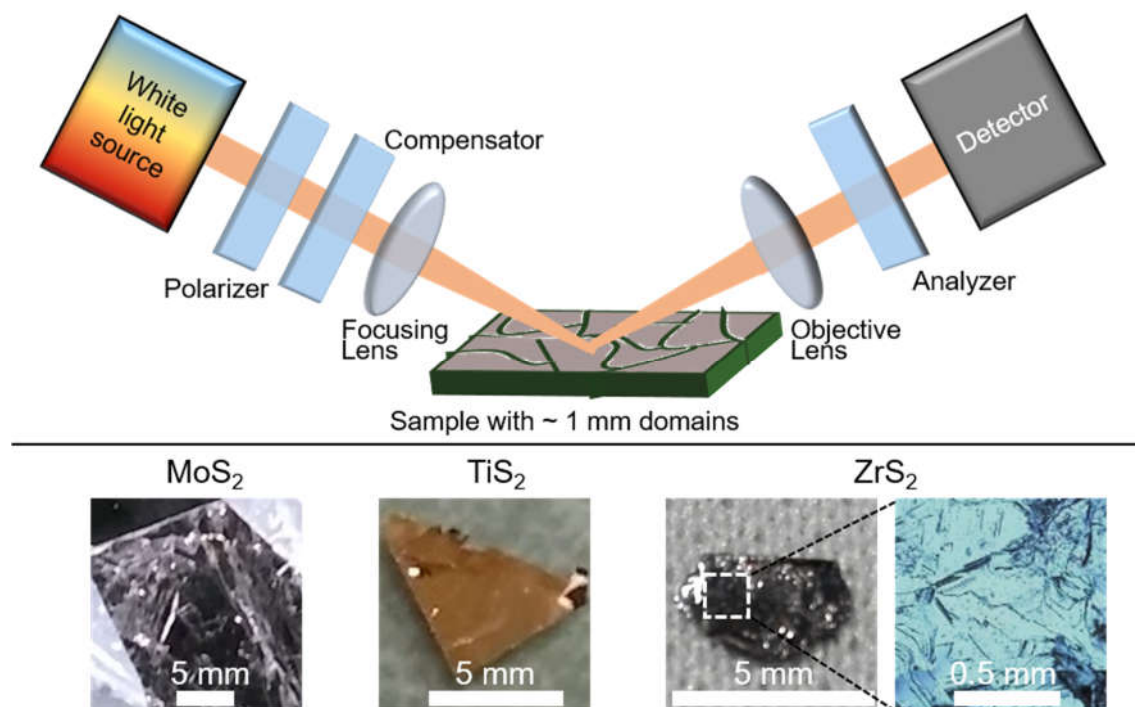
Figure S1: (a) Schematic of SE-2000 ellipsometry setup. Woollam VASE instrument performs similarly, but has an auto-retarder in place of the compensator, coupled with a rotating analyzer. **(b)** Low-magnification optical images of MoS_2, TiS_2 and ZrS_2 bulk crystals with different sized reflective facets. Higher magnification image (of dotted white box) of ZrS_2 is shown, clearly showing facets and heterogeneous nature of surface.

In **Figure S1(b)** we show optical images of bulk TMD crystals measured here. We chose sufficiently-thick pieces of naturally-occurring MoS_2 (Smithsonian Institution, naturally-occurring molybdenite, catalog number NMNH B3306; and 2D Semiconductors) to reduce back reflections. The surface had ~ 1 mm scale reflective facets, which necessitated the use of focusing optics. TiS_2 was purchased from 2D Semiconductors (grown using flux technique) and had large reflective domains ~ 5 mm. ZrS_2 was purchased from 2D Semiconductors, grown using flux zone method, and had a surface similar to MoS_2, with reflective domains ~ 1 mm. MoS_2 was measured using both Semilab and Woollam ellipsometers, with similar results; TiS_2 was measured using the Woollam ellipsometer, and ZrS_2 was measured using the Semilab ellipsometer.

S2. Attributing peaks to different transitions

Figure S2 shows the experimentally-measured imaginary part of relative permittivity (ϵ_2) for all TMDs under study (effective permittivity). The solid lines show the actual permittivity,

determined by analyzing the ellipsometry data taking into account the native oxide layers, using the model explained in Section IV. We label the discrete optical transitions by transition metal and subscript (for example A-exciton transition in $MoS_2 \sim M_A$). In Table S1, we attribute peaks in ϵ_2 to particular optical transitions discussed in earlier literature.
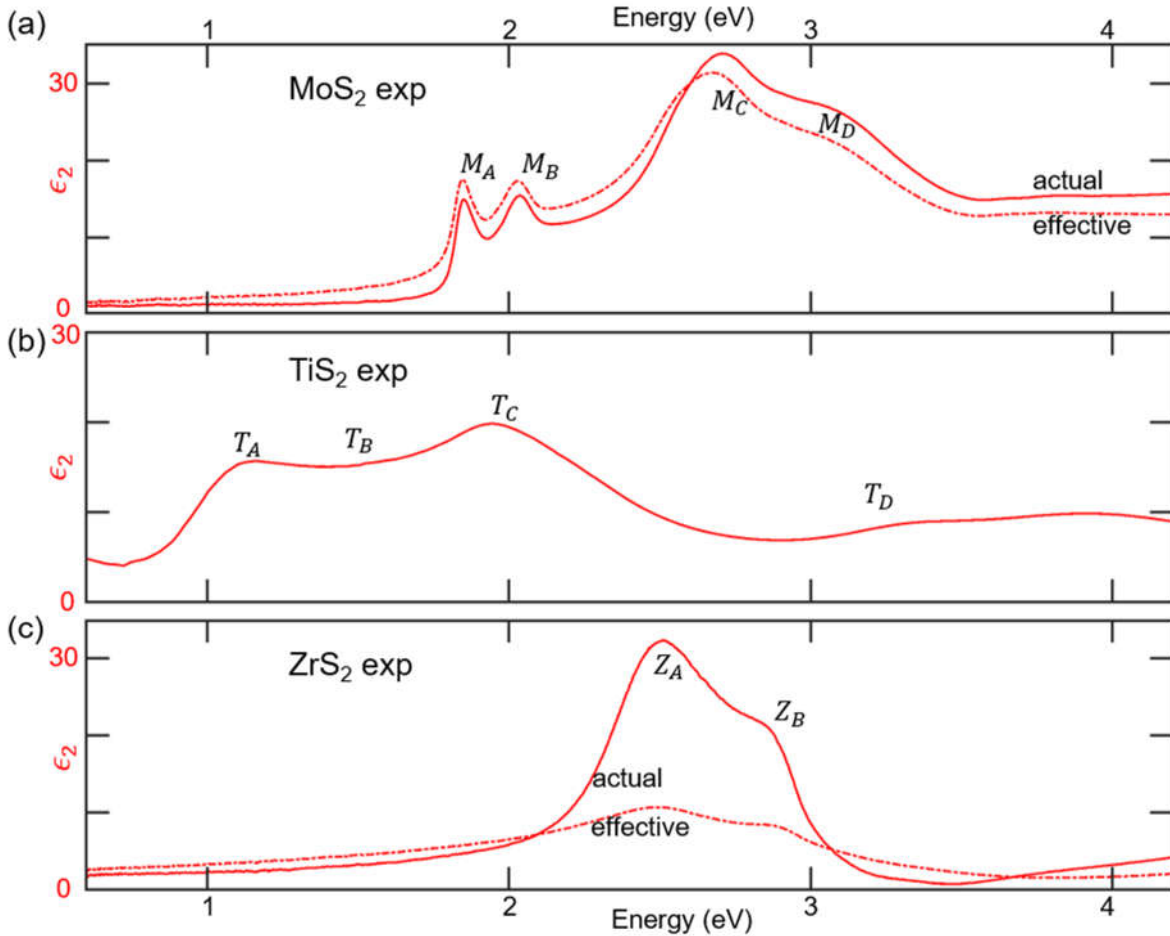
Figure S2: Imaginary part of experimentally measured relative permittivity for **(a)** MoS_2, **(b)** TiS_2 and **(c)** ZrS_2 ($AOI = 70°$). The different optical transitions are indicated by the transition metal and subscript. The solid lines show the actual permittivity, determined by analyzing the ellipsometry data taking into account the native oxide layers; the dashed lines show the effective permittivity, not accounting for the native oxide.

TMD	Peak and energy (eV)	Possible origin or literature
MoS₂	A ~ 1.8 eV	A Exciton, Ref [47]
	B ~ 2.1 eV	B Exciton, Ref [47]

	C $\sim$ 2.7 eV	C Exciton (band-nesting), Ref [47]
	D $\sim$ 3.1 eV	D Exciton, Ref [47]
TiS$_2$	A $\sim$ 1.1 eV	Ref [34]
	B $\sim$ 1.5 eV	Ref [34]
	C $\sim$ 1.9 eV	Possible 2 peaks, Ref [34]
	D $\sim$ 3.2 eV	Possible 2 peaks, Ref [34]
ZrS$_2$	A $\sim$ 2.5 eV	Possible 2 excitonic peaks, Ref [34]
	B $\sim$ 2.9 eV	Possible 2 excitonic peaks, Ref [34]

Table S1: Spectral peaks observed in experimentally measured ϵ_2 attributed to different optical transitions for MoS$_2$, TiS$_2$ and ZrS$_2$. The experimental observations are also compared to previous literature.

S3. Transmission Electron Microscopy (TEM) characterization of surface

We used high-resolution TEM (HRTEM) and scanning TEM (STEM) to characterize the surface of bulk crystals. For TEM, we prepared cross-sectional samples via a gallium focused ion beam (FIB). We deposited a thin ($\sim$ 100 nm) amorphous carbon layer on top of the crystal for protection during subsequent FIB steps. Dark field (DF) STEM performed on MoS$_2$ (**Figure S3a**) indicates a slightly rough interface between carbon and underlying layered structure. HRTEM performed on TiS$_2$ (**Figure S3b**) shows a very sharp interface between FIB-deposited carbon and underlying crystals, and no overlayers. On the contrary, the ZrS$_2$ sample shows a thick amorphous layer on top of the pristine crystalline structure (**Figure S3c**).
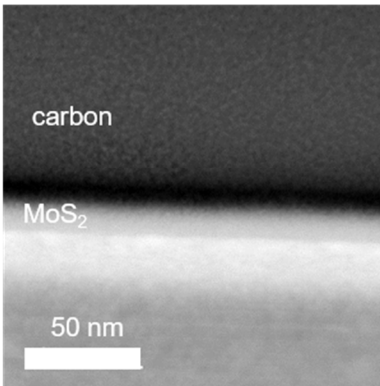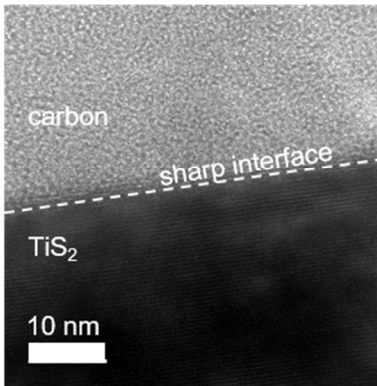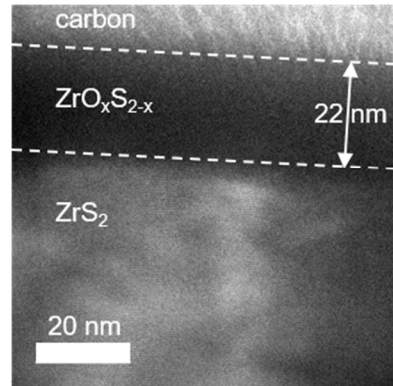
Figure S3: High-resolution TEM and STEM for sulfides. The carbon is deposited by focused ion beam instrument for protection of underlying crystalline material. a) Dark-field (DF) STEM for MoS_2 sample shows slightly rough interface between FIB-deposited carbon and underlying MoS_2. b) HRTEM for TiS_2 sample shows sharp interface between deposited carbon and underlying crystalline TiS_2. c) HRTEM for ZrS_2 sample shows amorphous overlayer on underlying crystalline ZrS_2.

### S3b. Energy-dispersive X-ray spectroscopy (EDS) of MoS_2 and ZrS_2 top surfaces

To characterize the elemental composition of observed amorphous layers and top surface for MoS_2 and ZrS_2, we performed high-resolution energy-dispersive X-ray spectroscopy (EDS) on the cross-sectional samples. In **Figure S4** we present integrated intensities of characteristic X-ray peaks corresponding to carbon, transition metal (molybdenum/zirconium), sulfur and oxygen. For MoS_2, the interface is fairly sharp (**Figure S4a**), and there is a distinct lack of oxygen in the underlying crystals. For ZrS_2, the amorphous layer observed via HRTEM has a higher (lower) value of oxygen (sulfur/zirconium) compared to underlying pristine layers (**Figure S4b**). Qualitatively, we assign an average composition of 50% sulfur – 50% oxygen to this layer.
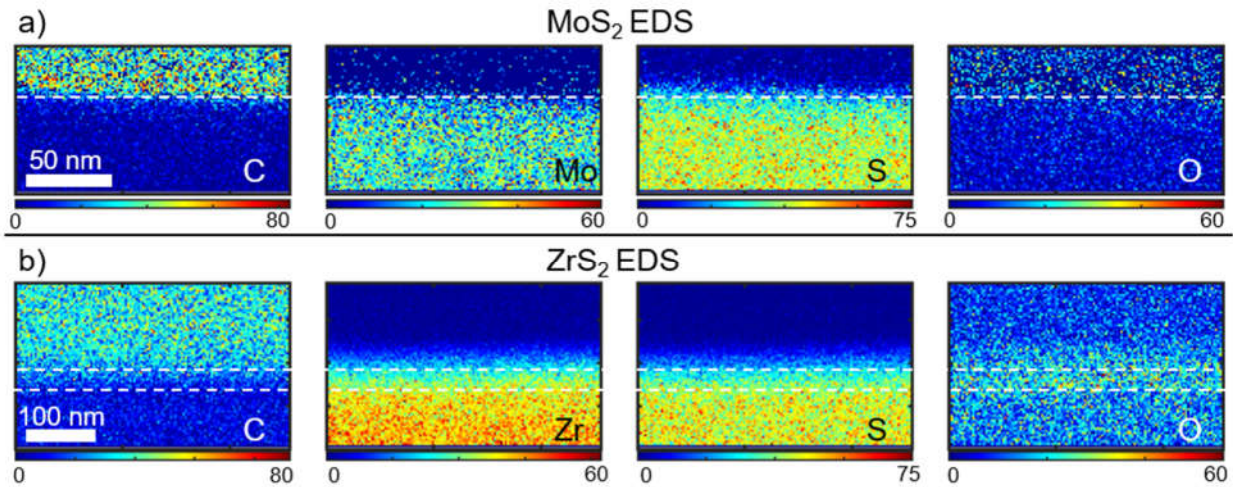
Figure S4: EDS characterization of cross-sectional samples of a) MoS_2 and b) ZrS_2. The $K_{\alpha1}$ lines are characteristic of the different elements (carbon, molybdenum/zirconium, sulfur and oxygen). The X-ray peaks are integrated to improve signal to noise.

S4. Oxide and roughness modeling

TEM measurements show the presence of a moderately rough layer for MoS_2, with root-mean-square roughness approximately 2 nm (measured by atomic force microscopy, not shown here). Therefore, **Equation 3** cannot be directly used: we require an optical model incorporating different layers including this roughness layer. We define an optical model for the MoS_2 sample in **Figure S5a**. Similarly, we present in **Figure S5b** an optical model for the ZrS_2 sample, incorporating a 20 nm overlayer. We perform modeling using software provided by Semilab and J. A. Woollam; both give similar results. We show modeling results in **Figures 1, 2 and S2**.
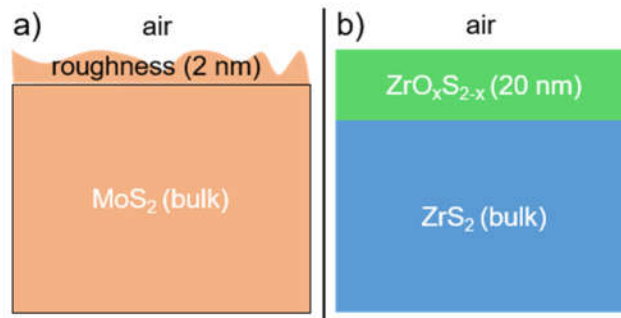
Figure S5: Schematic of the layer structure used for modeling raw ellipsometry data. a) MoS_2 data modeling incorporates a roughness layer of thickness $\sim$ 2 nm on top of bulk MoS_2. b) ZrS_2 data modeling incorporates a zirconium oxy-sulfide layer (thickness $\sim$ 20 nm) on top of bulk ZrS_2.

S5. TiS_2 measured with and without focusing optics

Focusing optics for a small analysis spot size are necessary to avoid simultaneously measuring multiple, small surface patches (with different tilts), which can mix of polarization. However, focusing optics themselves can result in small amount of depolarization, and a change in the measured relative permittivity.[27] In **Figure S6** we show that the measurements on TiS_2 using broad-beam mode (3 mm spot size) and focusing-beam mode (0.3 mm spot size) are quantitatively similar. Thus the focusing mode can be used without introducing error in the measurements. Note that such a comparison is only possible for TiS_2, since MoS_2 and ZrS_2 have very small ($\sim$ 1 mm) reflective domains, and therefore cannot be measured in broad-beam mode.
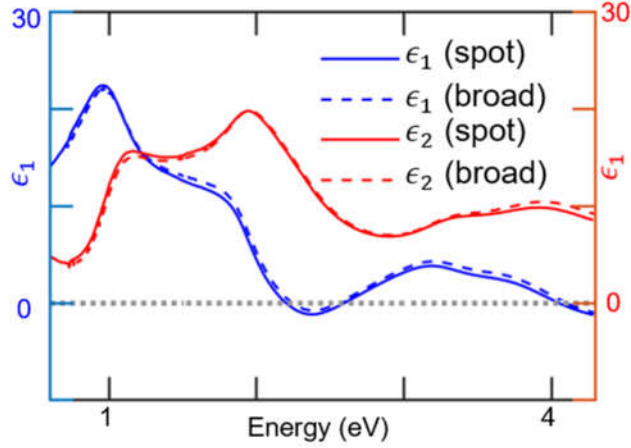
Figure S6: Comparison of relative permittivity measured via focused beam (spot) and broad beam (broad) for TiS_2 ($AOI = 70°$). The measurements are quantitatively similar, thus demonstrating focusing mode is suitable for ellipsometric measurements.

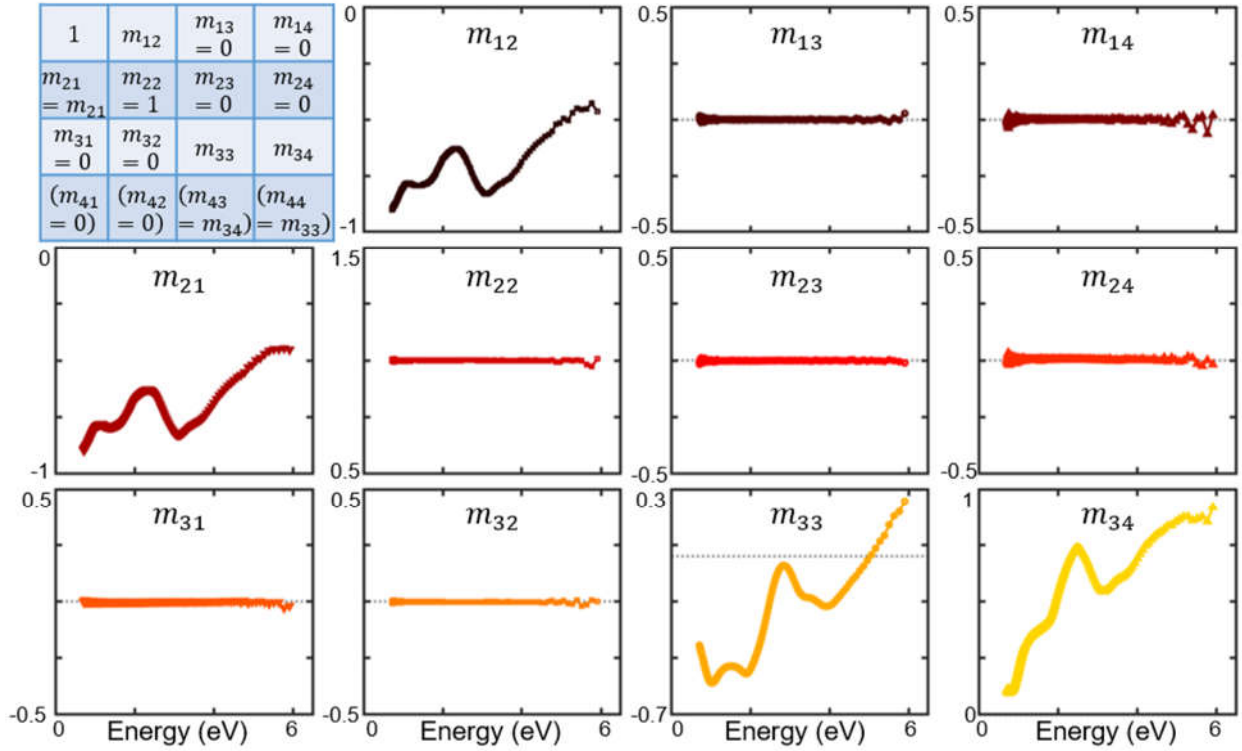## S6. Mueller matrix (MM) measurement

Equation 1 assumes no cross-polarization components, which can result from asymmetries in the material. A more general form of the reflection matrix can be defined with help of Jones matrix (S):

$$S = \begin{bmatrix} r_{pp} & r_{ps} \\ r_{sp} & r_{ss} \end{bmatrix} \Rightarrow \rho = \begin{bmatrix} \rho_{pp} & \rho_{ps} \\ \rho_{sp} & 1 \end{bmatrix}. \tag{S1}$$

The cross-polarization components are measured by ρ_{ps} and ρ_{sp}. Experimentally, these components can be measured by using Mueller matrix (MM) formalism (a.k.a. generalized ellipsometry), which measures the complete dielectric polarization of a material.[48,49] The symmetry of the MM provides information about the optical symmetry of the material, such as the orientation of the birefringent optical axis relative to the incidence plane of the measurement.[48,50]

In the main text we present results for electric field polarized in the plane of the layered TMDs. These measurements assume that the materials under study are birefringent, with the optical axis out-of-plane. We turn to MM measurements to explicitly measure the position of optical axis. MM provides the complete dielectric polarization of a material, and can measure cross-polarization components and depolarization effects due to surface layers.[49,51] In **Figure S7** (top left) we show the expected MM for a birefringent material, with the optical axis parallel to plane of incidence.

Due to symmetry, certain elements are expected to be zero, while others should be repeated.[48,50] We carry out measurements on TiS$_2$ at AOI = 70°. With the experimental configuration of a rotating compensator and auto-retarder (using Woollam UV-NIR Vase), the last row of the MM is not measurable.[27] We find that the measurements match the expected symmetry of a MM corresponding to a birefringent material with optical axis in plane of incidence. Thus, the optical axis for TiS$_2$ points out-of-plane, with high in-plane rotational symmetry. MoS$_2$ shows similar behavior (determined using Semilab SE-2000, data not shown here).

Figure S7: Mueller matrix (MM) ellipsometry on 1T-TiS$_2$. The table (top left) shows the symmetry expected from for a birefringent material with optical axis parallel to plane of incidence. The measurements (m_{12} *etc.*) support this symmetry. The last row of MM is not measurable with the rotating compensator configuration used here. All components are normalized to m_{11}.

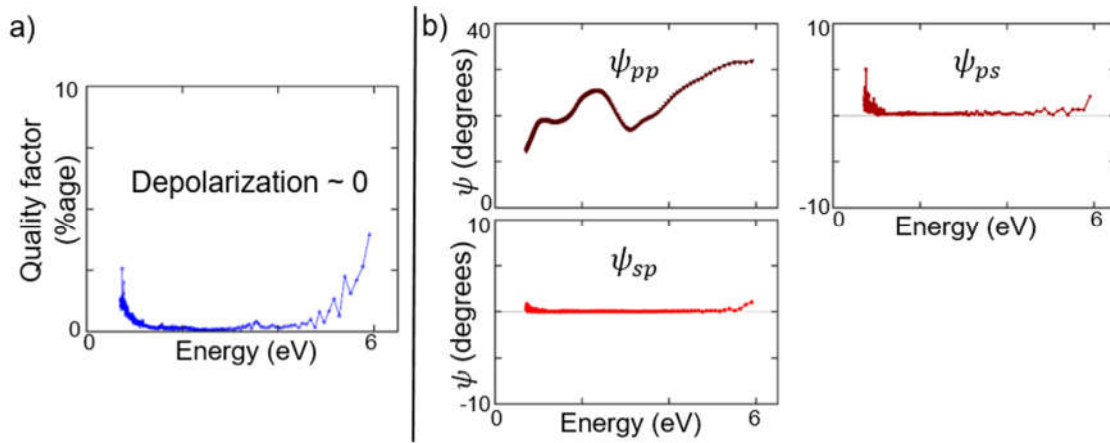## S7. The equivalence between the Mueller matrix (MM) and the Jones matrix (S)

MM provides the complete polarization state of a material. In the case of no depolarization, a MM can be converted into an equivalent Jones matrix (S):

$$MM \rightarrow S = \begin{bmatrix} r_{pp} & r_{ps} \\ r_{sp} & r_{ss} \end{bmatrix} \Longrightarrow \rho = \begin{bmatrix} \rho_{pp} & \rho_{ps} \\ \rho_{sp} & 1 \end{bmatrix} \qquad (S2)$$

The Jones matrix explicitly indicates any cross-polarization conversion, and is simpler to understand

This conversion $MM \rightarrow S$ can be quantified with a quality factor related to depolarization. We find that quality factor (depolarization) is indeed ~ 0 for TiS$_2$ (consistent with minimal surface roughness for TiS$_2$, (**Figure S8(a)**)), indicating that the measured MM is a pure MM.[48,49] Thus, the conversion $MM \rightarrow S$ can be carried out (**Figure S8(b)**). The cross-polarized (off-diagonal) components of S are ~ 0, indicating minimal polarization conversion.

Figure S8: Conversion of the Mueller matrix (MM) to the equivalent Jones matrix (S) for TiS$_2$ ($AOI = 70°$). (a) Quality factor quantifying the $MM \rightarrow S$ conversion. The quality factor is analogous to a depolarization measurement. (b) Diagonal and off-diagonal components of equivalent S. Here, only ψ is plotted (see equation 1 of main text). All components are normalized to ρ_{ss}. Off-diagonal components are ~ 0.

S8. Theoretical calculations (DFT) for out-of-plane relative permittivity

Layered materials are expected to have large anisotropy due to the weak inter-layer bonding. Using DFT, we calculate both the out-of-plane ($\epsilon_{\parallel}$, electric field parallel to the c-axis) and the in-plane relative permittivity ($\epsilon_{\perp}$, electric field perpendicular to the c-axis, as shown in **Figure 1** and discussed in the main text) for all three TMDs under study. In **Figure S9** we plot together $\epsilon_{\parallel}$ and $\epsilon_{\perp}$ for comparison. The calculated $\epsilon_{\parallel}$ is much smaller than $\epsilon_{\perp}$ (*c.f.* **Figures 1 and S2**). Thus, we predict a large anisotropy (*i.e.* giant birefringence) between in-plane and out-of-plane directions, and these layered materials can be explored for optical modulators and polarization converters.
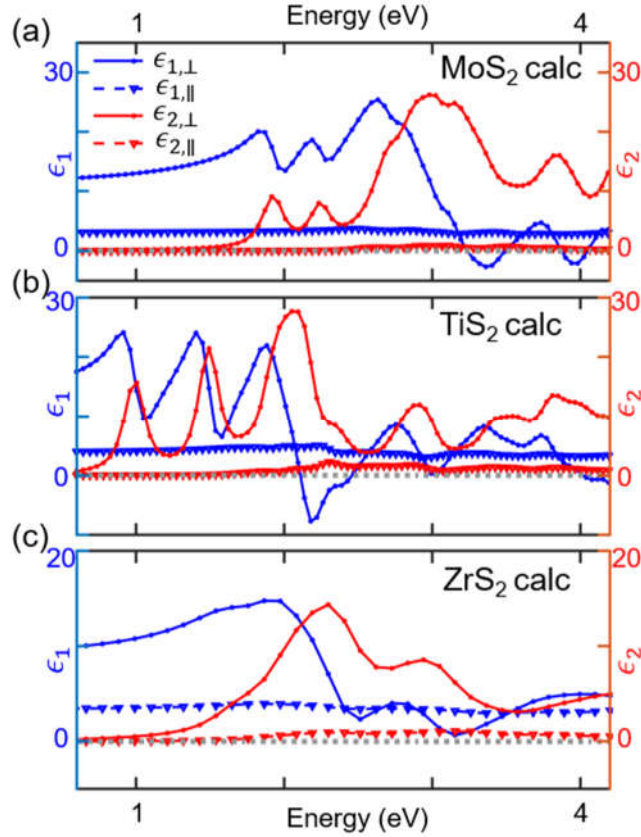
Figure S9: Comparison of calculated relative permittivity for electric field in-plane ($\epsilon_\perp$, electric field perpendicular to the c-axis, solid line with circular markers) and out-of-plane ($\epsilon_\parallel$, electric field parallel to the c-axis, dotted line with triangular markers) for **(a)** MoS_2, **(b)** TiS_2 and **(c)** ZrS_2. $\epsilon_\parallel$ is much smaller than $\epsilon_\perp$, giving rise to giant birefringence.

S9. Multiple angle-of-incidence (MAI) measurements

To separate $\epsilon_\perp$ and $\epsilon_\parallel$, measurements at more than one AOI are needed. Measurements at low AOI are insensitive to $\epsilon_\parallel$, and high AOI is usually needed to measure $\epsilon_\parallel$. We carry out MAI measurements for MoS_2 and TiS_2; in **Figure S10** we show the real part of the effective (measured) relative permittivity (ϵ_1). DFT calculations suggest a low $\epsilon_\parallel$, and suggest an increase in effective ϵ with increase in angles. The lack of measured changes in effective ϵ_1 for higher AOI (for MoS_2, TiS_2) is thus puzzling. However, after explicitly measuring the direction of optical axis (via MM), we realize that even at high AOI, the measurement of effective ϵ is only weakly dependent on $\epsilon_\parallel$ for materials with such high index. Thus, MAI measurements are unable to uncouple $\epsilon_\perp$ and $\epsilon_\parallel$ due to high index and absorption. In the next section, we calculate effective ϵ for a range of $\epsilon_\perp$

and $\epsilon_\parallel$, and for different AOI, and predict changes of only a few percent with different AOI (below signal to noise of our setup). A way forward is to perform MAI measurements on the side-plane of polished and thick TMD crystals, where the optical axis will depend on sample rotation, and anisotropy will be extractable.[52]
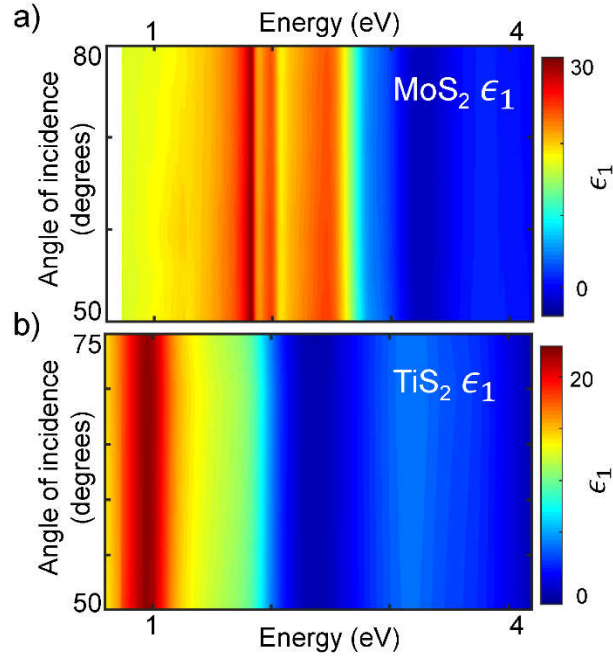
Figure S9: MAI measurements, plotting ϵ_1 for (a) MoS$_2$ and (b) TiS$_2$. No noticeable change is measured between low and high incidence angles due to the large refractive index of the materials, which strongly refracts incident light along the optical axis.

S10. Effective ϵ for a range of $\epsilon_\perp$ and $\epsilon_\parallel$, and for different angle of incidence (AOI)

MAI measurements did not reveal a significant change in effective ϵ for any of the materials measured here (MoS$_2$, TiS$_2$, ZrS$_2$). With the optical axis confirmed to be out-of-plane, we carry out calculations for $n_{effective} (= \sqrt{\epsilon})$ for a range of in-plane ($n_\perp$) and out-of-plane ($n_\parallel$) refractive indices. Fresnel coefficients for a uniaxial material can be written as

$$r_{pp} = \frac{n_\perp * n_\parallel * cos(\Phi) - n_i * \left(\left(n_\parallel^2 - \left(n_i * sin(\Phi) \right)^2 \right)^{\frac{1}{2}} \right)}{n_\perp * n_\parallel * cos(\Phi) + n_i * \left(\left(n_\parallel^2 - \left(sin(\Phi) \right)^2 \right)^{\frac{1}{2}} \right)} \qquad (S3)$$

$$r_{ss} = \frac{n_i * cos(\Phi) - \left(n_\perp^2 - (n_i * sin(\Phi))^2\right)^{\frac{1}{2}}}{n_i * cos(\Phi) + \left(n_\perp^2 - (n_i * sin(\Phi))^2\right)^{\frac{1}{2}}} \qquad (S4)$$

, where $n_i, n_\perp, n_\parallel$ are ambient, in-plane and out-of-plane refractive (real part) indices respectively, and Φ is angle of incidence.[28] Subsequently, an $n_{effective}$ can be defined and calculated using the ellipsometric ratio ($\rho = r_{pp}/r_{ss}$) followed by ϵ using

$$\epsilon = sin^2(\Phi) * \left(1 + tan^2(\Phi) * \left(\frac{1-\rho}{1+\rho}\right)^2\right) \Rightarrow n_{effective} = real(\sqrt{\epsilon}) \qquad (S5)$$

In **Figure S11** we plot $n_{effective}$ for a range of $n_\perp$ and $n_\parallel$, using realistic values for the imaginary part of the refractive index (k). We choose two representative AOIs, 5° and 70° (**Figure S11(a,b)**), to illustrate the change of $n_{effective}$ with different $n_\perp$ and $n_\parallel$ for fixed $k = 1$. However, the difference between $n_{effective,5°}$ and $n_{effective,70°}$ is very small (**Figure S11(c)**) and within experimental confidence limits. Thus, multiple AOI measurement may not be suitable for these high-index and absorptive materials. We also calculate the index difference for the case of $k = 0$, and observe a measurable (~ 0.4) change in $n_{effective}$. Thus, for a transparent highly anisotropic material, multiple AOI measurements may be able to measure the anisotropy.
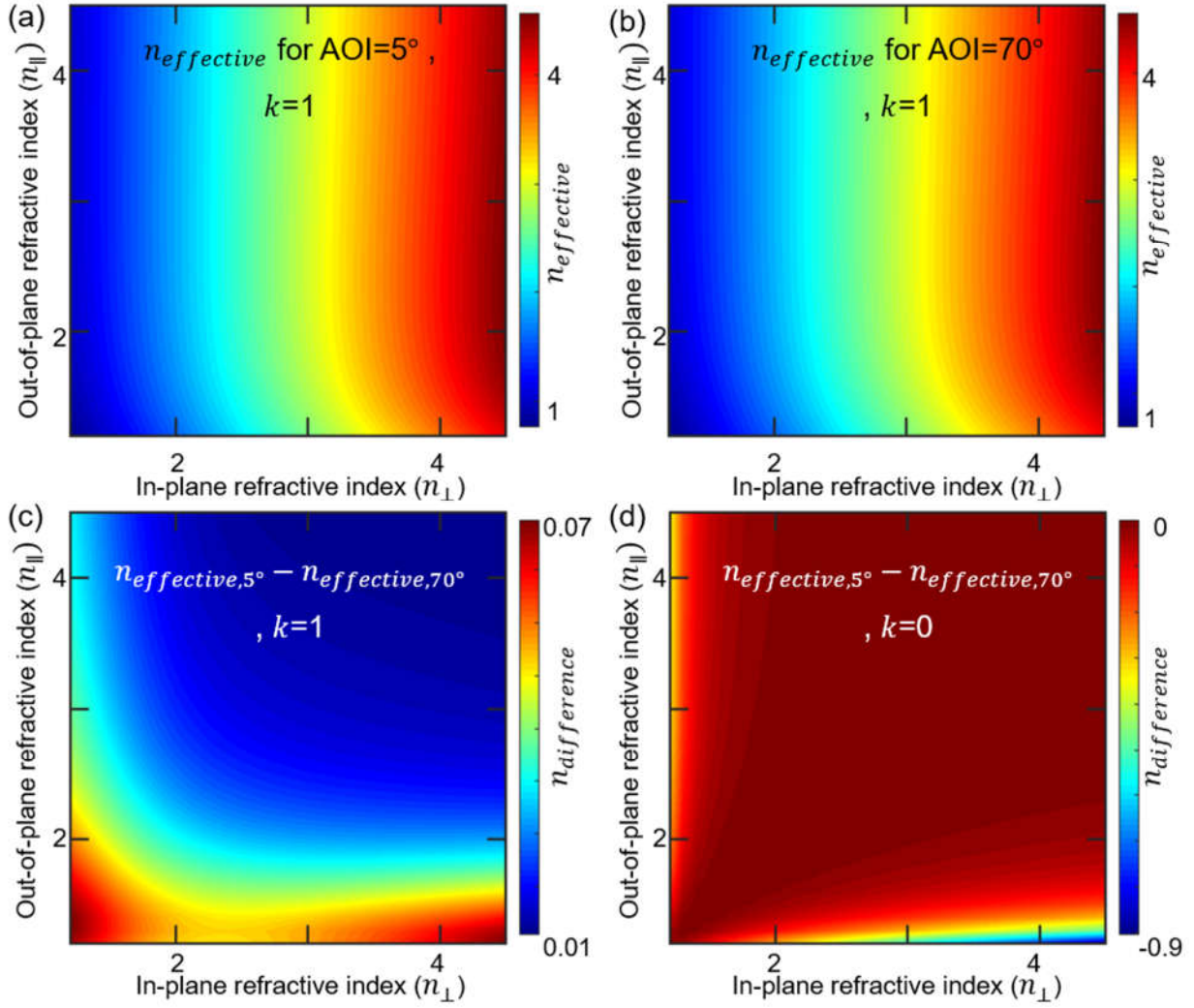
Figure S11: Calculation of $n_{effective}$ for a range of $n_{\perp}$ and $n_{\parallel}$, and for different AOI. **(a)** $k = 1$, $\Phi = 5°$. **(b)** $k = 1$, $\Phi = 70°$. **(c)** $n_{effective,5°} - n_{effective,70°}$, for $k = 1$. **(d)** $n_{effective,5°} - n_{effective,70°}$, for $k = 0$.

S11. Details of DFT calculations

Some details of DFT are provided in the main text, and are supplemented here. For the dielectric function calculation, $10 \times 10 \times 5$ Monkhorst-Pack k-point mesh and fully relaxed unit cell are used for reasonable accuracy.[53] Following our previous work, we predict ion-clamped dielectric functions within the random phase approximation (RPA)[35,36] with the equation:

$$\epsilon_{\alpha\alpha}(\omega) = 1 - \lim_{q \to 0} \left(\frac{4\pi e^2}{q^2 \Omega}\right) \sum_{c,v,k} w_k \times \frac{\left|\langle u_{v,k}|u_{c,k+q_\alpha}\rangle\right|^2}{E_{c,k} - E_{v,k} - \hbar\omega - i\zeta} \quad (\alpha = x, y, z) \quad (S6)$$

c and v indicate the conduction band states and valence band states respectively, $|u_{n,k}\rangle$ is the cell-periodic part of the wave functions of the band-n at k, Ω is the volume of the simulation supercell, w_k is the k-point weight and ζ is a phenomenological damping parameter (taken to be 0.025 eV).

Our DFT results are in qualitative agreement with the experiments results (**Figure 2**). However, we note that the DFT-calculated electronic band structure (Kohn-Sham eigenvalues) suffers from systematic errors, and methods beyond the independent particle picture are required for better accuracy.

S12. Phase diagram calculations

We calculate the Gibbs free energy of pure phases and alloys using DFT and the quasi-harmonic approximation (QHA) method, aided by Phonopy code.[54–56] We use the QHA to calculate phonon spectra, which can be approximated as quantum harmonic oscillators at fixed lattice constant, and the vibrational entropy. To this entropy we add a configurational entropy term, although this term is dwarfed by the vibrational entropy. The steps involved in phase diagram calculations are provided below:

1) Fully relaxed volume: Alloy metal sulfides are simulated in 2×2×2 (1T phase) and 2×2×1 (2H phase) supercells, thus each supercell contains 8 formula units. By varying the composition of 8 metal atoms in each supercell, we investigate 5 stoichometries (TiS_2, $Ti_{0.75}Mo_{0.25}S_2$, $Ti_{0.50}Mo_{0.50}S_2$, $Ti_{0.25}Mo_{0.75}S_2$, MoS_2) in two phases (2H and 1T). We choose a Monkhorst-Pack k-point mesh of size 3×3×2, and we tested convergence up to size 10×10×5. We relax each supercell without any symmetry constraints using the conjugate gradient method, and we manually perturb the initial positions of ions to promote the gradient descent.

2) Relaxation with Fixed volume: At given phase and stoichiometry, we strain every fully-relaxed supercell by 0.5% in each vector, up to 2.5% in both compression and tension, to generate 11 different volume points. We relax each point under similar conditions but with fixed volume.

3) Phonon spectra: We calculate the dynamical matrix of each supercell for fixed phase, stoichiometry and volume using the Parlinski-Li-Kawazoe method, combining the DFT simulation

results of a set of displaced supercells in which one ion is displaced by 0.01 Å. We calculate the phonon spectra and density by solving non-zero eigenvalue dynamical matrices. The Helmholtz free energy (F) then follows directly from the partition function (Z) of phonon vibrations:

$$Z = \prod_{qv} \frac{\exp(-\hbar\omega(qv)/(2k_B T))}{1 - \exp(-\hbar\omega(qv)/(k_B T))} \qquad (S7)$$

$$F = -k_B T \ln Z = \frac{1}{2}\sum_{qv} \hbar\omega(qv) + k_B T \sum_{qv} \ln\left[1 - \exp\left(-\frac{\hbar\omega(qv)}{k_B T}\right)\right] \qquad (S8)$$

q is the wave vector and v is the band index. For all phonon spectra calculations we use a 15×15×15 q-point mesh.

4) Calculate the Gibbs free energy: We calculate the Gibbs free energy (at given phase and stoichiometry under 0 Pa pressure) by minimization of the sum of Helmholtz free energy and pV, which only depends on volume under fixed temperature:

$$G(T,p) = \min_V\left[U(V) + F_{phonon}(T,V) + pV\right] \qquad (S9)$$

$U(V)$ is the DFT-calculated ground state energy. The configuration entropy term from Mo-Ti alloy is also added to the final results, but the contribution is in the scale of 0.1 eV, which is negligible.

$$S = -k_B \sum_{n=1}^{W} P_n \ln P_n$$

The contribution of the pV term is also negligible since it is ~ 1 meV when pressure ~ 1 atmosphere.

S13. Comparison of complex permittivity for MoS₂ from different published sources

In **Figure S12** we compare our experimental results for the complex dielectric constant of MoS₂ to select, previously-published experimental results on bulk and monolayer samples.[32,57] We find considerable variation in the magnitude of ϵ_1 and ϵ_2 between two representative papers, one using reflection ellipsometry (Ref[32]), and the other using transmission measurements (Ref[57]). Regarding bulk crystals, our work and Ref[32] are qualitatively similar, though the magnitude is

different. We suggest that the difference in magnitude could be due to our accounting for the native oxide layer in this work.
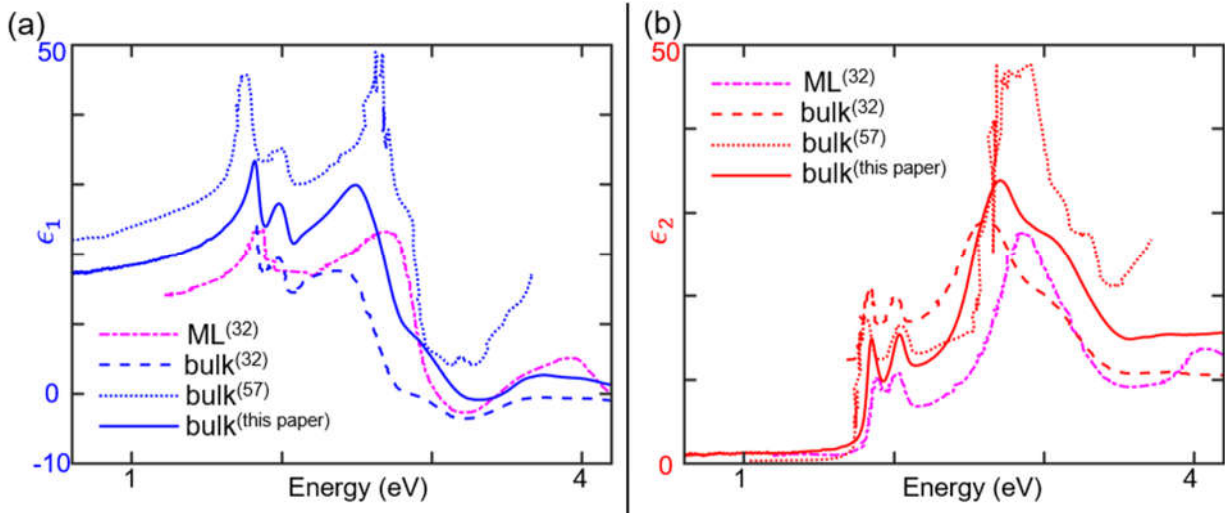
Figure S12: Comparison of published measurements of the in-plane complex relative permittivity of MoS_2 at room-temperature, both bulk and monolayer. (a) Real component ε_1. (b) Imaginary component ε_2. Ref [32] is based on ellipsometry, while Ref [57] is based on transmission measurements.

Supplementary References

[47] R.F. Frindt and A.D. Yoffe, Proceedings of the Royal Society of London Series A-Mathematical and Physical Sciences **273**, 69 (1963).
[48] J.W. Hovenier, Appl. Opt., AO **33**, 8318 (1994).
[49] J.J. Gil and E. Bernabeu, Optica Acta: International Journal of Optics **32**, 259 (1985).
[50] O. Arteaga, Thin Solid Films **571**, 584 (2014).
[51] D.A. Ramsey and K.C. Ludema, Rev. Sci. Instrum. **65**, 2874 (1994).
[52] W.Y. Liang, Journal of Physics C: Solid State Physics **6**, 551 (1973).
[53] H.J. Monkhorst and J.D. Pack, Physical Review B **13**, 5188 (1976).
[54] A. Togo, L. Chaput, I. Tanaka, and G. Hug, Physical Review B **81**, 174301 (2010).
[55] M. Youssef, B. Yildiz, and K.J. Van Vliet, Physical Review B **95**, 161110(R) (2017).
[56] A. Togo and I. Tanaka, Scripta Materialia **108**, 1 (2015).
[57] R.A. Neville and B.L. Evans, phys. stat. sol. (b) **73**, 597 (1976).